Crystal Growth and Physical Properties of Orthorhombic Kagome Lattice Magnets RFe₆Ge₆ (R=Y, Tb, Dy)

Abhijeet Nayak, 1, 2, * Sk Jamaluddin, 1, 2 Fan Wu, 1, 2 Emily Rapp, 3 Resham Babu Regmi, 1, 2 Mohamed El Gazzah, 1, 2 Bence G. Márkus, 1, 2 László Forró, 1, 2 Madhav P. Ghimire, 4, 5 Allen Oliver, 6 Kateryna Foyevtsova, 1, 2 Igor I. Mazin, 7, 8 and Nirmal J. Ghimire 1, 2 Department of Physics and Astronomy, University of Notre Dame, Notre Dame, IN 46556, USA 2 Stavropoulos Center for Complex Quantum Matter, University of Notre Dame, Notre Dame, IN 46556, USA 3 Physics, Astronomy and Materials Science Department, Missouri State University, Springfield, MO 65897, USA 4 Central Department of Physics, Tribhuvan University, Kirtipur, Kathmandu 44613,, Nepal 5 Leibniz Institute for Solid State and Materials Research, IFW Dresden, Helmholtzstr. 20, D01069 Dresden, Germany 6 Department of Chemistry & Biochemistry, University of Notre Dame, Notre Dame, IN 46556, USA 7 Department of Physics and Astronomy, George Mason University, Fairfax, VA 22030, USA 8 Quantum Science and Engineering Center, George Mason University, Fairfax, VA 22030, USA (Dated: November 24, 2025)

Kagome magnets represent a promising class of materials that exhibit intriguing electronic and magnetic properties, and they have recently garnered significant attention. While most kagomelattice compounds are hexagonal, here we report the single-crystal growth and physical property measurements of similar compounds RFe_6Ge_6 (R = Y, Dy, Tb), which crystallize in an orthorhombic structure. The structure can be derived from a hexagonal prototype RFe₃Ge₂ by replacing every other R atom with a covalent Ge₂ dimer. Ordering of the latter makes the structure orthorhombic the kagome net slightly distorted, and the three Fe sites formally inequivalent. The iron and rare-earth sublattices order independently: the Fe moments order above 400 K having, with ferromagnetic Kagome planes stacked antiferromagnetically, while the rare-earth moments order below 9 K. While TbFe₆Ge₆ exhibits a single magnetic ordering transition associated with the Tb atoms, DyFe₆Ge₆ shows two distinct magnetic phase transitions, which are strongly influenced by crystal electric field effects on the Dv³⁺ ions. Density functional theory (DFT) calculations show that the ferromagnetic ordering of the Fe planes is driven by a high density of states at the Fermi energy. They also reveals three dramatically different structural energy scales: R and Ge₂ form alternating 1D chains perpendicular to the kagome planes, and violating this alternation incurs a huge energy cost. Aligning these chains is less costly, and actual 2D order of anti-aligned chains costs very little. These compounds represent a unique class of materials, offering new possibilities to investigate the interplay between the distinct crystal lattice geometry and the underlying electronic and magnetic properties.

I. INTRODUCTION

Kagome magnets have emerged as a central focus in condensed matter research due to their intriguing electronic and magnetic properties [1, 2]. Recently, it has been recognized that even subtle deviations from an ideal kagome lattice can give rise to novel and exotic physical phenomena. For instance, breathing kagome lattices host electronic and magnetic topological states [3– 5], while twisted kagome lattice compounds exhibit electronic topological phases and spin-ice-like behavior [6–8]. More recently, RTi₃Bi₄ compounds have drawn attention for their distinctive electronic and magnetic properties [9–14]. These compounds feature a distorted kagome net of Ti atoms combined with zigzag chains of R atoms, an arrangement believed to produce magnetic and electronic characteristics distinct from those of other kagome-based materials.

Among the most extensively investigated kagome systems are the RT_6X_6 compounds, commonly referred to as R166, where R is a rare-earth element, T is a transition metal, and X is Sn or Ge. These materials exhibit a remarkable variety of emergent magnetic and electronic behaviors [15–37]. Generally, the R166 compounds crystallize in the HfFe₆Ge₆-type structure [Fig. 1(a)] with hexagonal symmetry (space group P6/mmm), in which the T atoms form a regular kagome network.

However, several members of this family, particularly the $R\text{Fe}_6\text{Ge}_6$ compounds, form superstructures derived from an average hexagonal structure with lattice parameters $(a, c)_h$. When transformed into the orthohexagonal setting, where the axes are redefined as $(c, \sqrt{3}a, a)_h$, these superstructures adopt distinct forms depending on the specific rare-earth element [38–42]. Compounds with R = Y, Tb, Dy, and Ho crystallize in the TbFe₆Sn₆-type structure with orthorhombic symmetry (space group Cmcm) as depicted in Fig. 1(b). The emergence of this superstructure originates from the ordered arrangement of R and Ge atoms within the Fe–Ge host

^{*} Corresponding author: anayak@nd.edu

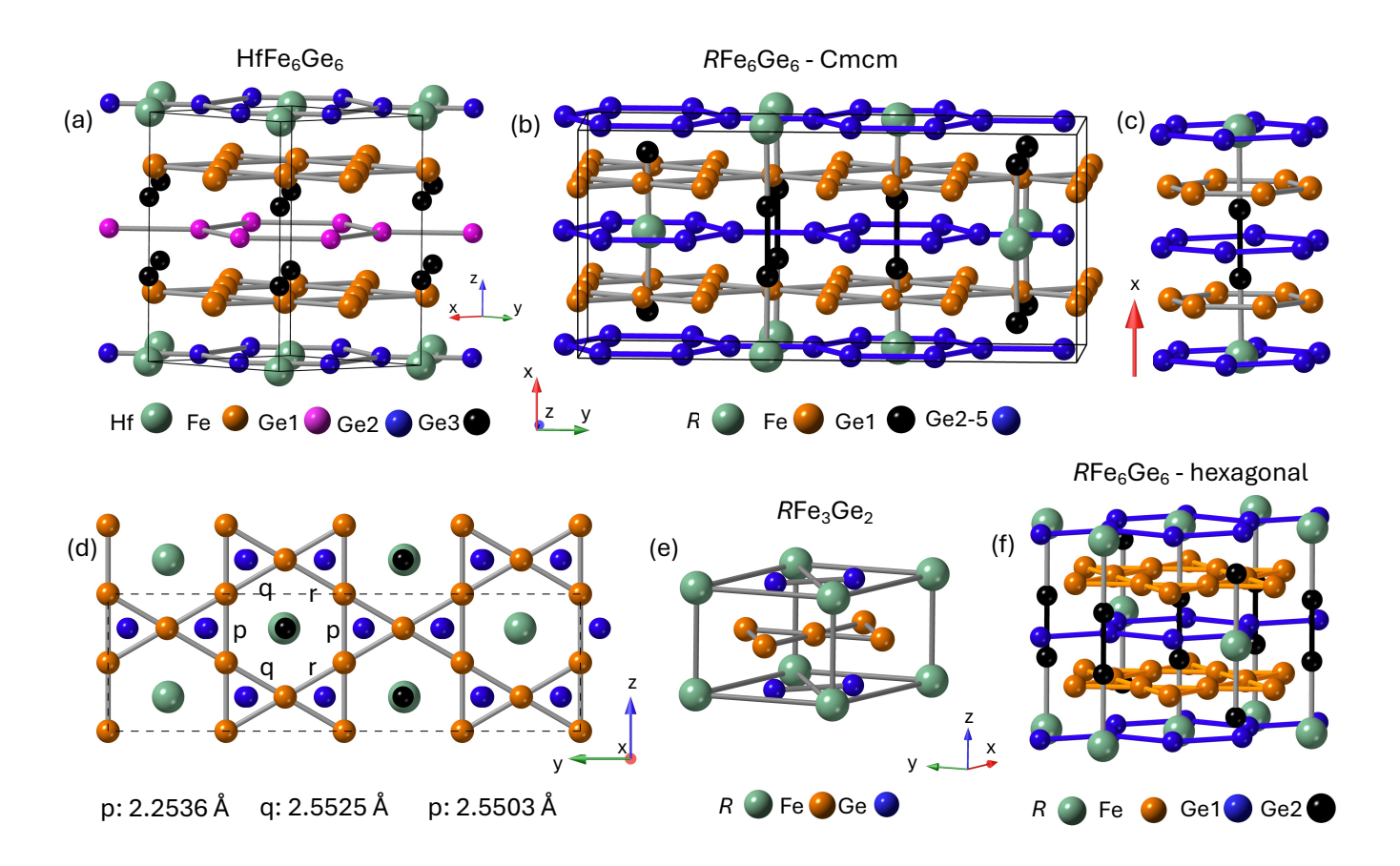


FIG. 1: a) Sketch of HfFe₆Ge₆-type crystal structure. b) Crystal structure of RFe₆Ge₆ in the Cmcm space group. There are five inequivalent Ge atoms. A different color (black) is used for Ge1 to highlight its dimerization along a-axis. Other Ge atoms (Ge2-5) are all represented by blue colored balls. c) Ge-Ge dimers forming linear chains with R atoms along the a-axis penetrating the Ge honeycomb and Fe kagome planes. d) a-axis view of the TbFe₆Ge₆-Cmcm structure highlighting the kagome network of Fe atoms. The bond lengths of atoms forming the kagome network slightly distorted due to the orthorhombic symmetry. The letters p, q, and r denote equivalent bond lengths within each kagome unit, as indicated in the legend. e) Sketch of a RFe₃Ge₂ unit cell, a building block for the hexagonal RFe₆Ge₆ structure. f) Schematic illustration of the formation of RFe₆Ge₆ structure from doubling of RFe₃Ge₂ (details are provided in the introduction section). The solid black lines in panels (a) and (b) and the dashed lines in panel (d) represent the unit cell of the corresponding crystal structures.

lattice. Consequently, these materials exhibit intricate structural characteristics, featuring a slightly distorted kagome network of Fe atoms within the crystallographic a-plane as presented in [Figs. 1(b,d)], and chains of R-Ge dimers oriented perpendicular to the kagome nets as noted in [Figs. 1(b,c)].

It is helpful to compare the RFe_6Ge_6 -Cmcm structure with the better-studied HfFe $_6Ge_6$ -type structure. In both structures, Fe forms a Fe $_3$ kagome network, with its hexagonal voids filled by Ge (Ge h). In HfFe $_6Ge_6$, the R site forms a triangular layer Hf t , followed by a Ge (Ge h) [see Fig. 1(a)]; these stack in the sequence Hf $^tGe_2^h$ -Fe $_3Ge^t$ -Ge $_2^h$ -Fe $_3Ge^t$ -Hf $^tGe_2^h$, yielding the overall composition HfFe $_6Ge_6$.

The RFe_6Ge_6 -Cmcm structure is derived from another hexagonal lattice, RFe_3Ge_2 as shown in Fig. 1(d). This parent structure has the same symmetry group as

 $HfFe_6Ge_6$, but consists of only two layers: $R^tGe_2^h$ - Fe_3 . The RFe₆Sn₆-Cmcm structure emerges when the prototype unit cell of RFe₃Ge₂ is doubled along the hexagonal c-axis, and every other R atom is replaced by a tightly bound Ge_2 dimer (bond length ~ 2.4 Å), yielding the overall composition of RFe₆Ge₆. This produces RGe₂ chains that penetrate the hexagonal channels of the kagome network, as illustrated in Fig. 1(f). However, because R and Ge_2 have different shapes, it is sterically unfavorable for all Rs to lie in one plane, and all Ge₂s dimers in another. Instead, they adopt a staggered arrangement within the hexagonal basal plane (which becomes bc plane in Cmcm notation). It is well known that a triangular plane cannot be partitioned 1:1 without breaking the hexagonal symmetry; accordingly, the structure becomes orthorhombic. The precise pattern of intraplanar ordering of R and Ge_2 is more subtle. Ex-

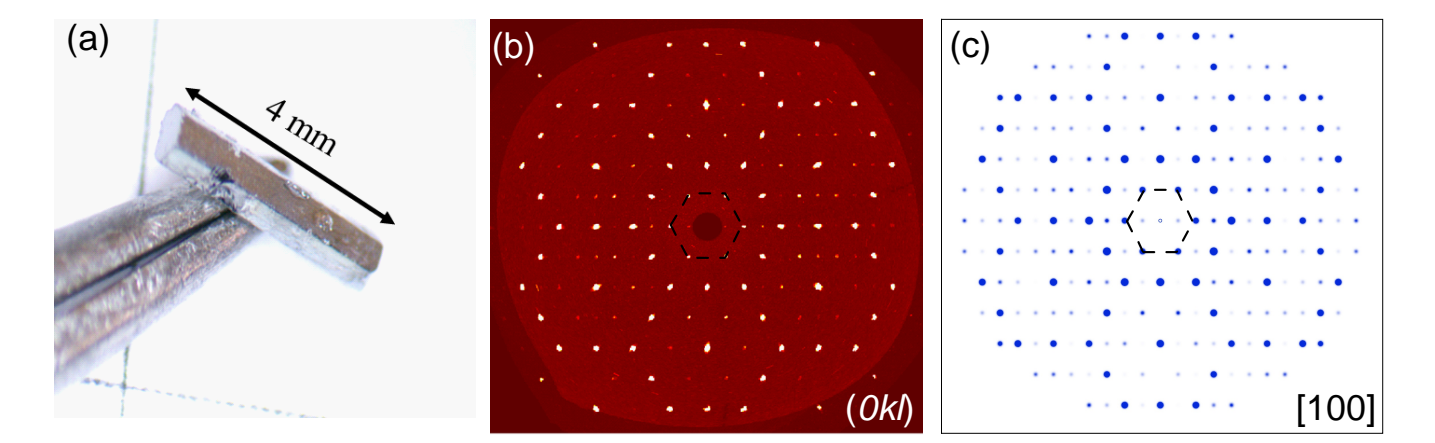


FIG. 2: a) Optical microscope image of a representative TbFe $_6$ Ge $_6$ single crystal mounted on the tip of tweezers. b) Reciprocal space map of the (0kl) scattering plane obtained via single-crystal X-ray diffraction, confirming the in-plane crystallographic order and symmetry of the DyFe $_6$ Ge $_6$ structure. c) Simulated single-crystal diffraction pattern of DyFe $_6$ Ge $_6$ along the [100] direction, for comparison with the experimental data shown in panel (b). The dashed hexagons in panels (b) and (c) serve as visual guides.

perimentally, these sites are often disordered (although the 1D order inside each chain is strictly maintained).

The Cmcm RFe₆Ge₆ compounds have previously been investigated in polycrystalline form for their structural, magnetic and transport properties [38–42]. Here, we report the single-crystal growth of three members of this family with R = Y, Tb, and Dy, and present a comprehensive study of their structural, magnetic, transport, and electronic properties. Single crystal x-ray diffraction indicates that the samples are well ordered including the intraplanar R and Ge₂ chains, which adopt a specific (and unusual) double-stripe arrangement. In all three compounds Fe orders antiferromagnetically above 400 K. Tb and Dy exhibit ferromagnetic-like ordering below 20 K, whereby Dy shows two low-temperature magnetic transitions with a complex magnetic character. All three compounds are metallic and each displays a distinct and intricate magnetoresistance. Analysis of low-temperature heat capacity of YFe₆Ge₆ reveals an unusually large Sommerfeld coefficient. Consistent with the ferromagnetic ordering in the planes, band-structure calculations for nonmagnetic YFe₆Ge₆ observe a large density of states at the Fermi level. DFT calculations also find the experimentally reported antiferromagnetic configuration to be energetically favorable; however, the resulting density of states in the magnetically ordered state is substantially reduced, more than four times smaller than expected based on the measured Sommerfeld coefficient. This behavior is reminiscent to the so-called "d-electron heavy fermion behavior", often observed in materials close a magnetic instability and ascribed to spin fluctuation [43– 45]. Our material is not close to a quantum critical point, but it is worth noting that such a behavior was recently reported in another strongly ordered compound [46], and tentatively ascribed to soft magnetic moments and longitudinal spin fluctuations. Observation of a similar trend

on YFe_6Ge_6 is interesting and deserves further studies. Unfortunately, in the Tb and Dy analogs the onset of low-temperature magnetic order prevents reliable extraction of Sommerfeld coefficients.

The combination of structural features, particularly the superstructure and orthorhombic distortion, with the large density of states at the Fermi level and enhanced Sommerfeld coefficient makes these compounds interesting for further study. In particular, tuning the Fermi level through chemical substitution may provide a promising route to explore the potential Fermi-surface instabilities in this family.

II. METHODS

Single crystals of RFe_6Ge_6 (R = Y, Tb, Dy) were grown using the self-flux method. Pieces of Y, Tb, or Dy (Thermo Scientific, 99.99%), Fe powder (Thermo Scientific, 99.999%), and Ge pieces (Thermo Scientific, 99.999%) were mixed in a molar ratio of 1:10:10, placed in an alumina crucible, and sealed in a fused silica ampoule under a vacuum of 10^{-3} Pa. The sealed ampoule was heated in a box furnace to 1200 °C over 10 hours, held at that temperature for 24 hours, then cooled to 1000 °C over 35 hours. It was subsequently reheated to 1050 °C over 10 hours, and without holding, cooled to 920 °C over 72 hours. At 920 °C, the ampoule was centrifuged to separate the crystals from the remaining molten flux. Several well-faceted, long needle-like crystals (see Fig. 2(a)) weighing up to 7 mg were obtained. The typical crystal dimensions are approximately 4 mm \times 0.5 mm \times 0.5 mm.

Single-crystal X-ray diffraction was performed to determine the crystal structure of all three $R\mathrm{Fe_6Ge_6}$ compounds. Data were collected on a silver-colored, block-

TABLE I: Crystallographic parameters for RFe ₆ Ge ₆	$_{3}$ compounds ($R = \text{Th}$	b, Dy, Y) at 250(2) K	ζ using Mo K α radiation.	Note
that the kagome plane is bc in this setting.				

Crystal system		Orthorhom	bic
Space group		Cmcm	
Temperature (K)		250(2)	
Wavelength (Å)		0.71073	
Z (formula units)		2	
$2\theta_{\min}$ (°)		4.61	
$2\theta_{\mathrm{max}}$ (°)		56.59	
Index ranges	$-10 \le h \le 1$	$10, -23 \le k$	$\leq 23, \ -6 \leq l \leq 6$
Compounds	YFe_6Ge_6	$\mathrm{TbFe_{6}Ge_{6}}$	DyFe_6Ge_6
Formula weight	1719.10	1859.12	1866.28
a (Å)	8.1134(3)	8.1379(3)	8.1193(2)
b (Å)	17.6662(7)	17.6975(6)	17.6699(6)
c (Å)	5.11650(10)	5.1257(2)	5.11910(10)
Volume ($Å^3$)	733.36(4)	738.21(5)	734.42(3)
Density (calc., g/cm ³)	7.785	8.364	8.439
$\mu \text{ (Mo K}\alpha) \text{ (cm}^{-1})$	433.73	447.68	455.43
Goodness of fit on F^2	1.179	1.141	1.347
$R(F)$ for $F^2 > 2\sigma(F^2)^a$	0.0155	0.0252	0.0245
$R_w(F^2)^{\mathrm{b}}$	0.0447	0.0775	0.0559

^a
$$R(F) = \sum ||F_o| - |F_c|| / \sum |F_o|$$

^b $R_w(F^2) = \left[\sum w(F_o^2 - F_c^2)^2 / \sum w(F_o^2)^2\right]^{1/2}$

shaped crystal with dimensions of $0.073 \times 0.068 \times 0.026$ mm³, using a Bruker Quest diffractometer equipped with a Bruker PHOTON III detector, and employing a combination of ω - and ϕ -scans with a step size of 0.5 degree [47]. The diffraction data were corrected for absorption and polarization effects and analyzed to determine the appropriate space group [48]. Structure solution was carried out using dual-space algorithms, followed by routine expansion of the initial model. Final structural refinement was performed using full-matrix least-squares analysis against F^2 values for all observed reflections [49]. All non-hydrogen atoms were refined with anisotropic atomic displacement parameters, and hydrogen atoms, unless otherwise noted, were placed in calculated positions. The extinction coefficient was also refined. Following data collection, a high-precision image of the (0kl)plane was captured [see Fig. 2(b)].

DC magnetization, resistivity, and heat capacity measurements were carried out using two separate Quantum Design Dynacool Physical Property Measurement Systems (PPMS) equipped with 9 T and 14 T magnets. The ACMS II option was used for DC magnetization measurements. Single crystals of $R\text{Fe}_6\text{Ge}_6$ were polished to appropriate dimensions for electrical transport measurements. Crystal orientation along the [100], [010], and [001] directions was determined using a Photonic Science X-ray Laue diffractometer to align the magnetic field along the a-, b-, and c-axes, respectively. Resistivity and Hall effect measurements were carried out using the standard four-probe method. Platinum wires (25 μ m in diameter) were used for electrical contacts, with contact resistances below 20 Ω . The electrical contacts were af-

fixed using Epotek H20E silver epoxy, and a 2 mA current was applied during transport measurements. To correct for contact misalignment, magnetoresistance and Hall resistivity data were symmetrized and anti-symmetrized, respectively, following the procedure described in Ref. [6]. All magnetic and magnetotransport data presented here were measured on multiple samples and found to be reproducible (see appendix for further data).

First-principles calculations were performed using the density functional theory (DFT) based on the WIEN2k code [50] using the augmented plane-wave basis set defined by the parameter $RK_{\rm max}=7.0$ and a $8\times8\times12$ mesh of k-points for Brillouin zone integration in a primitive two-formula-unit unit cell. Exchange and correlation effects were treated within the Perdew-Burke Ernzerhof gradient-corrected local density approximation [51].

III. RESULTS AND DISCUSSION

A. Crystal Structure

The compounds $R\mathrm{Fe_6Ge_6}$ crystallize in an orthorhombic structure characterized by the space group Cmcm (No. 63). At room temperature, the lattice parameters for different R atoms have been determined as follows: for R=Y, a=8.1134(3)Å, b=17.6662(7)Å, c=5.11650(10)Å; $R=\mathrm{Dy}$, a=8.1193(2)Å, b=17.6699(6)Å, c=5.1191(10)Å; and $R=\mathrm{Tb}$ a = 8.1379(3)Å, b = 17.6975(6)Å, c=5.1257(2)Å. A detailed summary of the single-crystal data and structural refinement parameters are provided in Table I, while fractional atomic coordi-

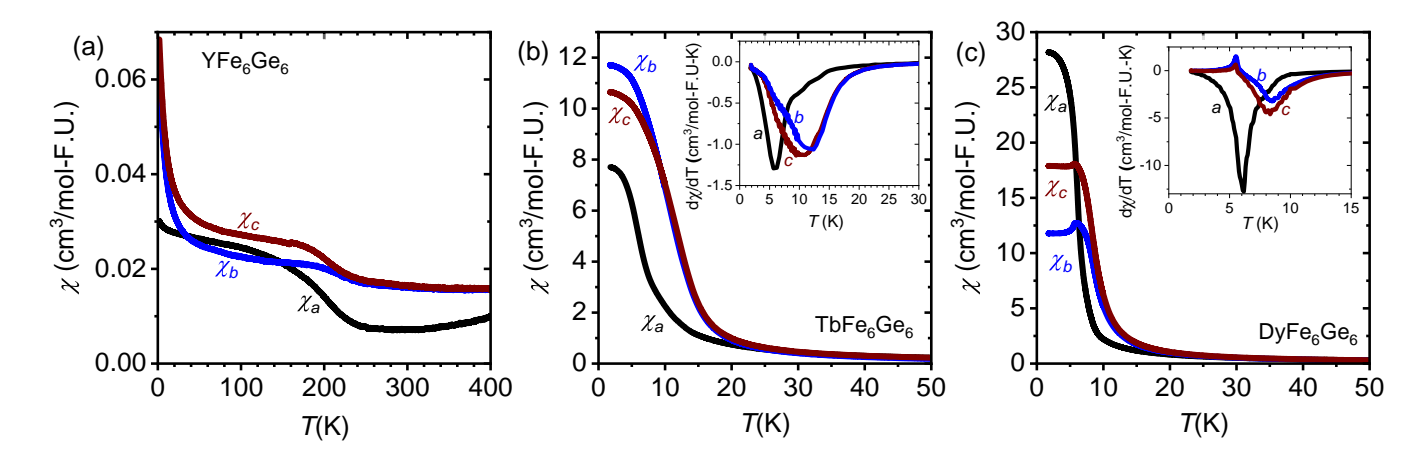


FIG. 3: Temperature dependence magnetic susceptibility (FC) measured at 0.1 T magnetic field along a (black line), b (blue line), and c (brown line) crystallographic axes for a) YFe₆Ge₆, b) TbFe₆Ge₆, and c) DyFe₆Ge₆. Insets in panels b and c show first derivative of corresponding FC magnetic susceptibility in all three crystallographic directions.

nates and equivalent isotropic displacement parameters are listed comprehensively in Table II for YFe₆Ge₆, and in appendix Table III, IV for TbFe₆Ge₆ and DyFe₆Ge₆, respectively.

TABLE II: Atomic coordinates, occupancy, displacement parameters and Wyckoff sites for YFe₆Ge₆ compounds.

Atom	Site	Occ.	x	y	z	$\mathrm{U}(_{eq})$
Y(1)	4c	1.000	0.00000	0.62710	0.75000	0.008
Ge(1)	8g	1.000	0.34708	0.62470	0.75000	0.008
Ge(2)	4c	1.000	0.00000	0.54202	0.25000	0.007
Ge(3)	4c	1.000	0.50000	0.70505	0.25000	0.007
Ge(4)	4c	1.000	0.50000	0.78957	0.75000	0.007
Ge(5)	4c	1.000	0.50000	0.45955	0.75000	0.007
Fe(1)	8e	1.000	0.24959	0.50000	0.50000	0.006
Fe(2)	8g	1.000	0.25036	0.62496	0.25000	0.006
Fe(3)	8d	1.000	0.75000	0.75000	0.50000	0.006

The orthorhombic unit cell of $R\text{Fe}_6\text{Ge}_6$ comprises four formula units (Z=4), totaling four R atoms, twenty four (Fe) atoms, and twenty four (Ge) atoms. Specifically, there is one crystallographically unique rare-earth atom sitting on 4c Wyckoff position, five distinct germanium atoms identified as Ge1 on the 8g site, and Ge2, Ge3, Ge4, and Ge5 which occupy distinct 4c sites, and three inequivalent iron atoms identified as Fe1 on the 8d site, Fe2 at the 8g site, and Fe3 at the 8e site.

Previous studies on polycrystalline samples of $R\text{Fe}_6\text{Ge}_6$ compounds have reported slight atomic disorder at the R (4c) site, characterized by a positional shift of 1/2 along the x-axis, as well as a similar disorder involving Ge atoms occupying 8g sites [39, 52, 53]. Considering the aforementioned literature results, we paid particular attention to examining possible disorder in our single crystal samples and therefore carried out structural refinements using three different approaches: i) assuming fully ordered Wyckoff positions, ii) allowing for

10% disorder between the rare-earth and Ge sites, and iii) allowing for 20% disorder. The refinement converged optimally when only the ordered atomic positions were used, yielding the lowest goodness-of-fit parameters (R_F and R_w), consistent with the discussion above and the DFT calculation, indicating that the R atoms and Ge dimers are perfectly well ordered in each 1D chain. It still leaves open the possibility of some 2D disorder between the ideal chains; to resolve this, one would need to go diffuse scattering.

The refined structural parameters are summarized in Table I (see also appendix Tables V-VIII, where the results of disorder refinement are summarized). These results indicate that our single crystals are better ordered than previously studied polycrystalline samples, reflecting a high degree of positional order within the 1D Y-Ge₂ chains. A precision pattern of (0kl) scattering plane of DyFe₆Ge₆ obtained from single crystal X-ray diffraction is presented in Fig. 2(b). For comparison, a simulated precision pattern of the same plane of DyFe₆Ge₆ is presented in Fig. 2(c).

B. Magnetic Properties

Magnetism in the $R\mathrm{Fe_6Ge_6}$ compounds has been extensively studied in polycrystalline samples. Experiments, including neutron diffraction, have established that the magnetic R and Fe sublattices order independently in these materials. The Fe sublattice exhibits antiferromagnetic order, with a Néel temperature (T_{N}) that remains essentially constant across the series, at approximately 485 K [40]. Neutron diffraction measurements on powders revealed that within each Fe kagome plane, the spins are aligned ferromagnetically, while adjacent planes couple antiferromagnetically along the a-axis, which is also the easy axis of magnetization [39–41].

The magnetic susceptibility χ of YFe₆Ge₆, measured

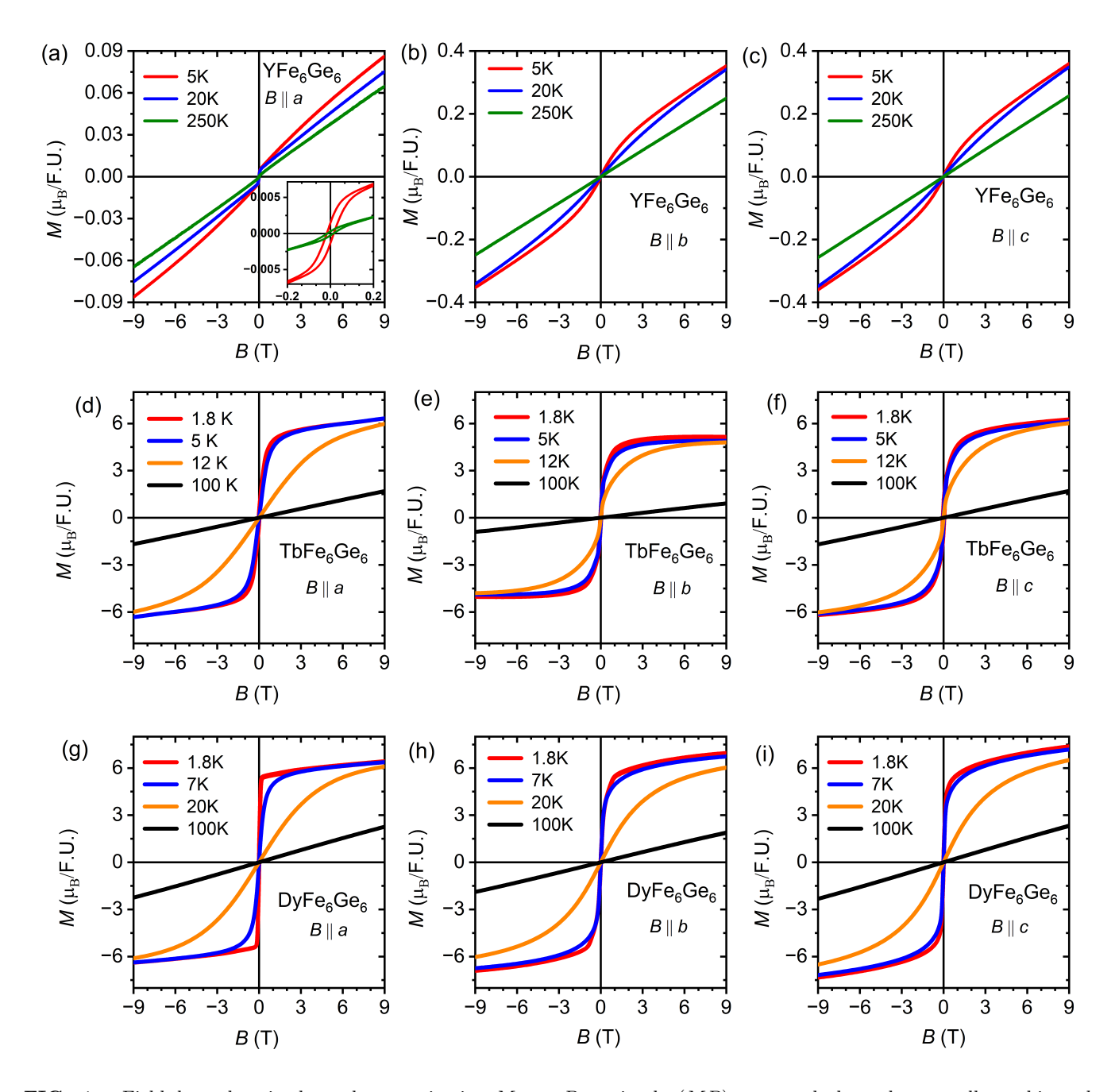


FIG. 4 : Field-dependent isothermal magnetization M vs. B or simply (MB) measured along the crystallographic a, b, and c axes for (a–c) YFe₆Ge₆, (d–f) TbFe₆Ge₆, and (g–i) DyFe₆Ge₆, respectively. Measurements were performed at various temperatures with an applied magnetic field sweeping from 9 T to –9 T and –9 T to 9 T.

under an external applied magnetic field B of 0.1 T along all three crystallographic directions, is shown in Fig 3(a). Since the Néel temperature $(T_{\rm N})$ lies above the measurement range of our PPMS, no clear feature associated with antiferromagnetic (AFM) ordering is observed. However, the overall low magnitude of χ is consistent with the AFM behavior. The field-cooled (FC) and zero-field-cooled (ZFC) curves show no divergence. A slight anomaly in χ is observed between 250 K and 200 K along all directions, which is rather unusual. For $B \parallel b$

and $B \parallel c$, this feature may indicate weak spin canting. However, for $B \parallel a$, where canting is symmetry-forbidden within the measurement geometry, this behavior suggests subtle complexity in the magnetic structure. Additionally, a small upturn in χ appears below 10 K for $B \parallel b$ and c, which may also be related to spin canting.

The complexity in magnetism is further observed in magnetization (M vs B) plots depicted in Figs. 4(a) -4(c). For B||a, there is a sharp slope change at around 0.1 T, with a small but clear hysteresis at 5 K, which

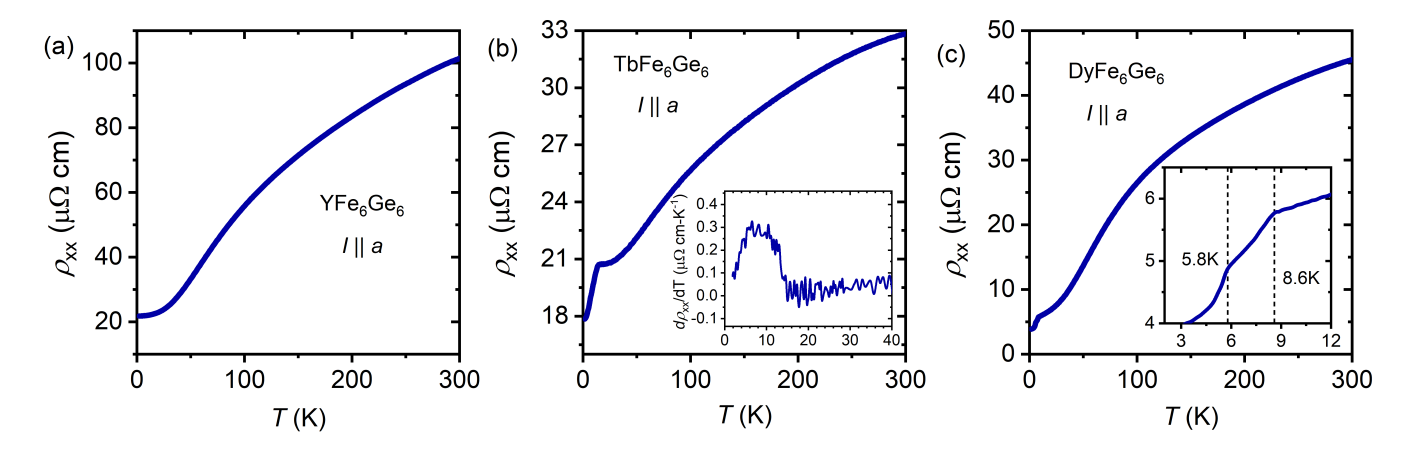


FIG. 5: Temperature variation of longitudinal resistivity measured with current applied along a-axis for a) YFe₆Ge₆, b) TbFe₆Ge₆, and c) DyFe₆Ge₆. Insets in panels (b) shows the temperature derivative of the resistivity and in panels (c) shows enlarge view of low temperature data.

survives up to 250 K (Fig. 4(a)). Magnetization for B||b,c is rather simple. At 5 K, in each direction, a small smooth curvature is observed in M-B curve, which is likely due to spin canting. The MB data at higher temperatures show straight line behavior as expected in an antiferromagnet.

Substituting the non-magnetic rare-earth element Y with magnetic R atoms does not significantly affect the Fe magnetic ordering; neither its transition temperature nor its magnetic structure. However, the R atoms themselves order magnetically at much lower temperatures. In TbFe₆Ge₆, Tb orders at 9 K, forming canted ferromagnetic layers in the a-plane that are stacked along the a-axis. This results in a net ferromagnetic component along the a-axis and an antiferromagnetic component along the c-axis [39, 40], indicating that the easy axis is canted away from the a-axis toward the c-axis. In DyFe₆Ge₆, Dy orders below 7.5 K, and the magnetocrystalline anisotropy shifts such that the easy-axis is now canted away from the c-axis toward the b-axis, yielding a ferromagnetic component along c and an antiferromagnetic component along b. This variation in magnetocrystalline anisotropy between the Tb and Dy compounds is attributed to higher-order (fourth and sixth) crystal field terms of the R^{3+} ions [53].

The magnetic susceptibility of TbFe₆Ge₆ is shown in Fig. 3(b). The susceptibility increases below about 20 K in each direction. However, there is no clear peak in any of them. The temperature derivative $d\chi/dT$, however, signals a broad decrease below 20 K, with an upturn at 5, and 9 K along a- and b,c-axes, respectively. Magnetization measurements shown in Fig. 4(d-f) show ferromagnetic behavior in each direction, with a small anisotropy. At 1.8 K, the moment along the b-axis shows saturation with a slightly smaller value (5 $\mu_{\rm B}/{\rm F.U.}$) compared to the moment along the a- and c-axes.

Likewise, magnetic susceptibility of DyFe₆Ge₆ is shown in Fig. 3(c). χ_a increases sharply below 10 K

while without any other sharp features at lower temperatures. On the other hand $d\chi_a/dT$, shows a sharp change at 6.2 K. χ_b and χ_c , increase rapidly below 15 K and show a marked peak near 5.5 K. Temperature derivative of these plots show an upturn at around 8.5 K and a peak at 5.5 K as shown in the inset of Fig. 3(c). These two magnetic transitions associated with Dy ordering is in contrast to a transition observed at 7.5 K in polycrystalline samples in the previous studies [53]. The magnetization data shown in Figs. 4(g-i) show ferromagnetic behavior along all three directions at 1.8 K, with a small anisotropy along the b-axis. The magnetization is not linear in B even at 20 K, likely due to the persistence of spin fluctuations is above the ordering temperature of Dy spins, and only demonstrate a linear behavior at 100 K, as expected for an antiferromagnet from the Fe sub-lattice. A similar temperature-dependent behavior is also seen in TbFe₆Ge₆.

C. Electrical Resistivity and Magnetoresistance

The temperature-dependent resistivity of all three compounds, measured with current along the a-axis (ρ_{xx} vs. T), is shown in Fig. 5. All three compounds exhibit metallic behavior. The residual resistivity ratio (RRR), defined as $\rho_{xx}(300 \text{ K})/\rho_{xx}(1.8 \text{ K})$, is 4.6 for YFe₆Ge₆, 1.8 for TbFe₆Ge₆, and 12.8 for DyFe₆Ge₆. The relatively low RRR of TbFe₆Ge₆ suggests that this compound may exhibit more disorder compared to the other two, although no such was detected in the single-crystal diffraction experiment. Interestingly, the residual resistivity of Y and Tb compounds are similar (20 $\mu\Omega$ -cm), while that of DyFe₆Ge₆ is much smaller (3.5 $\mu\Omega$ -cm).

As expected, YFe₆Ge₆ shows no distinct features in ρ_{xx} , consistent with its only magnetic transition occurring above 400 K. In TbFe6Ge₆, a sharp drop in ρ_{xx} is observed below 14 K, with a corresponding peak at 9 K

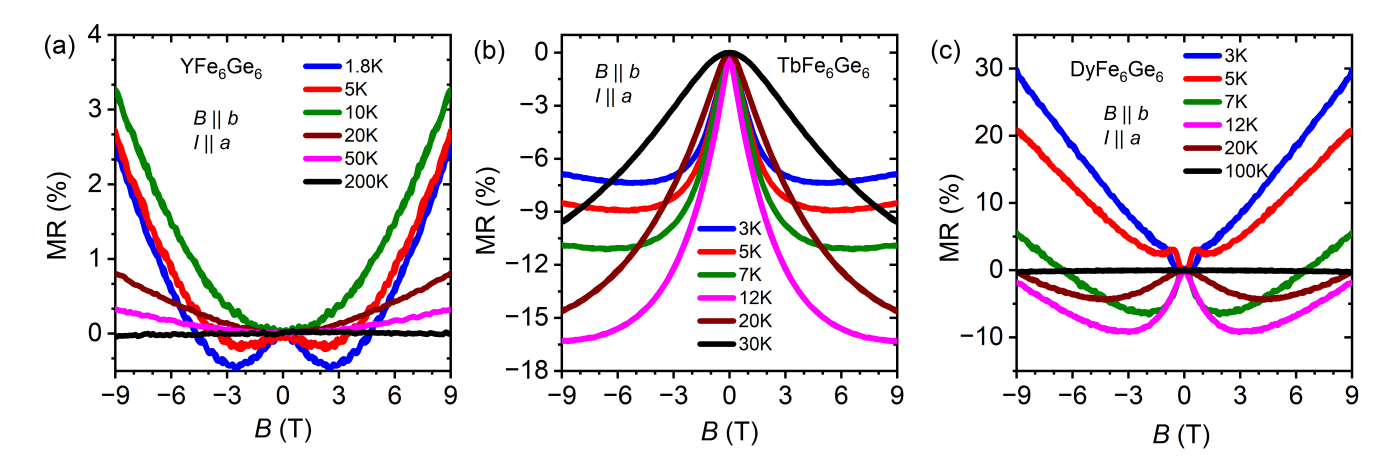


FIG. 6: Transverse magneto-resistance (MR) of a) YFe₆Ge₆, b) DyFe₆Ge₆, and c) TbFe₆Ge₆ measured with current (I) applied along a-axis and magnetic field (B) along b-axis.

in $d\rho_{xx}/dT$, consistent with the magnetic ordering of Tb atoms previously reported in polycrystalline samples [39]. DyFe₆Ge₆ exhibits two transitions in resistivity, at 8.6 K and 5.8 K (see inset of Fig. 5(c)), in agreement with the two transitions observed in the temperature derivative of magnetic susceptibility (see inset of Fig. 3(c)).

Magnetoresistance (MR) defined by:

$$MR = \left(\frac{\rho(B) - \rho(0)}{\rho(0)}\right) \times 100\%,$$

where $\rho(B)$ is the resistivity in an applied magnetic field B, and $\rho(0)$ is the resistivity measured in zero magnetic field, was measured with current along the a-axis and the magnetic field applied along the b-axis for all three compounds, as shown in Fig. 6. At low temperatures (e.g., 1.8 and 5 K), YFe₆Ge₆ exhibits negative magnetoresistance below approximately 3 T, which then becomes positive at higher fields. At 10 K, the MR is entirely positive. A similar trend, though with reduced magnitude, is observed up to 50 K. At 200 K, a very small negative MR reappears. This magnetoresistance behavior suggests that below 10 K, there is a ferromagnetic (FM) component, likely due to spin canting, as hypothesized from the susceptibility data in Fig. 3(a), which is suppressed by the external magnetic field, leading to negative MR. Once the FM component is fully suppressed, it becomes positive. The small negative MR observed at 200 K may have a similar origin, possibly related to the susceptibility anomaly seen around 250 K.

The MR of TbFe₆Ge₆ (Fig. 6(b)) is negative even up to 30 K, suggesting that fluctuation of Tb moments persists well above its ordering temperature. DyFe₆Ge₆, however, shows a very different behavior than both of Y and Tb compounds. The MR below 5 K is positive. At and above 7 K, it shows behavior similar to that of YFe₆Ge₆. This is quite strange for a system where the Dy moments are canted toward b-axis from c-axis. At low temperatures, there should be suppression of the fer-

romagnetic fluctuation due to the magnetic field applied along b-axis and one would expect negative magnetoresistance as in the case of Tb. This suggests that the magnetic structure is more complex than determined from the powder neutron diffraction, which is likely as the powder neutron diffraction does not pick up the two magnetic transitions observed in magnetic, transport and thermal (see below) measurements in single crystals of TbFe₆Ge₆.

D. Heat Capacity

The heat capacity of the RFe_6Ge_6 compounds (R = Y, Dy, Tb), plotted as C/T vs. T, is shown in Fig. 7. As depicted in Fig. 7(a), YFe₆Ge₆ does not exhibit any anomaly, consistent with the high-temperature antiferromagnetic ordering of the Fe moments. The electronic contribution to the heat capacity, γ , obtained from a linear fit to C/T vs. T^2 between 6 and 10 K using the expression $C/T = \gamma + \beta T^2$ [inset of Fig. 7(a)], produces a value of 84 mJ·mol-F.U.⁻¹·K⁻². We note an unusual flattening of the C/T vs T^2 data below 6 K; therefore, the fit was performed only above this temperature. We measured three samples from three different growth batches (the other two datasets are presented in the Appendix in Fig. 14), all giving consistent results. The density of states at the Fermi level, $N(E_{\rm F})$, estimated from this γ using the relation $N(E_{\rm F}) = 3\gamma/(\pi^2 k_{\rm B}^2 N_{\rm A})$, where $k_{\rm B}$ is the Boltzmann constant and $N_{\rm A}$ is Avogadro's number, is 35.7 states $\cdot \text{eV}^{-1} \cdot \text{F.U.}^{-1}$. This is more than four times the value obtained from DFT calculations in the antiferromagnetic state (see Fig. 8(b)), but im surprisingly good agreement with the result for the non-magnetic state (see Fig. 8(a)). The phonon heat capacity coefficient, β , is 0.22 mJ·mol-F.U.⁻¹·K⁻⁴. Note that had we taken the actual value of γ at $T \to 0$ instead of extrapolating the $T \gtrsim 6$ K data, we would get an even stronger, nearly sixfold, mass renormalization, placing

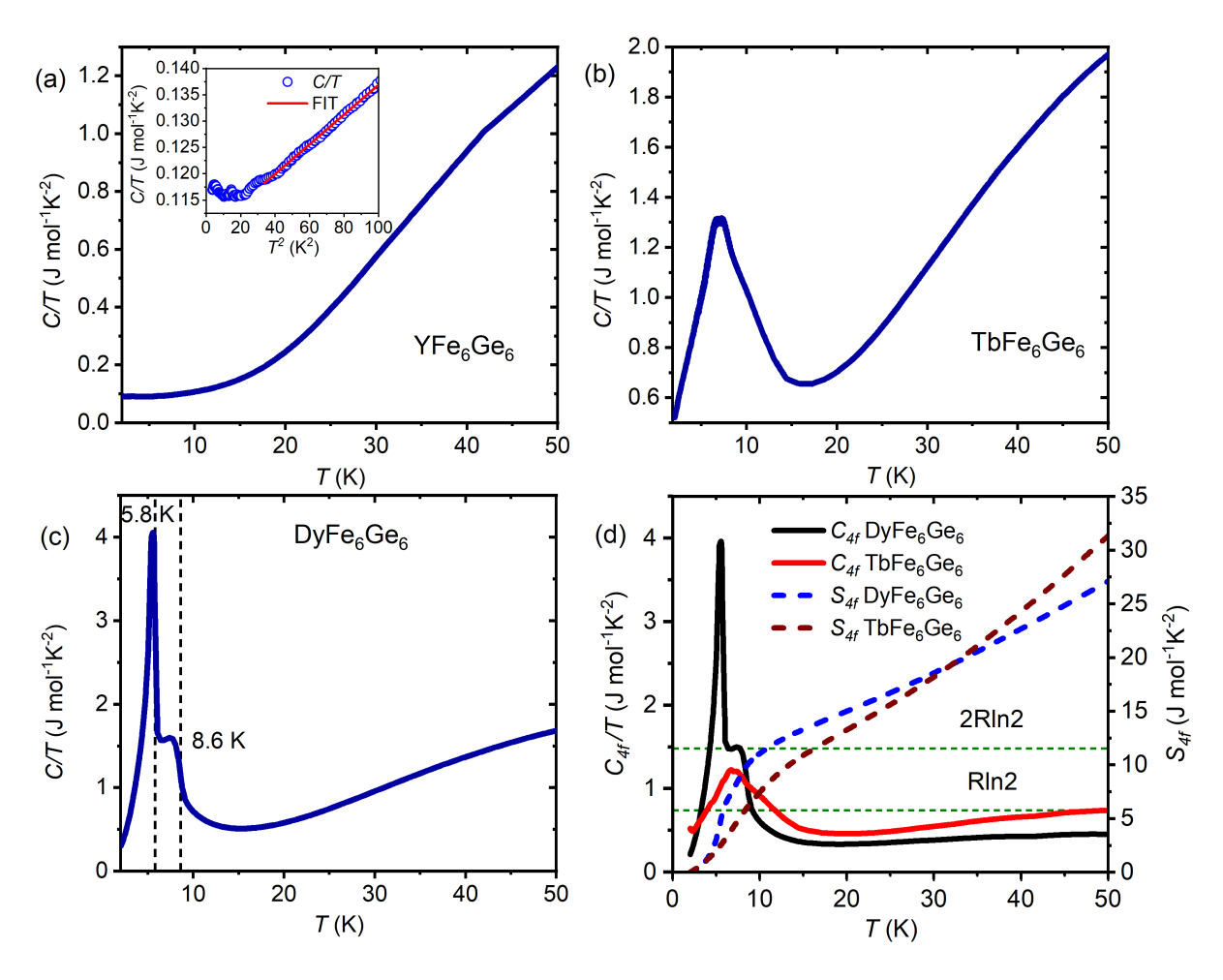


FIG. 7: Specific heat capacity divided by the temperature C/T of a) YFe₆Ge₆ (inset shows linear fit of C/T vs. T^2), b) TbFe₆Ge₆, and c) DyFe₆Ge₆. d) 4f contribution to the heat capacity $C_{4f}(T)$ of DyFe₆Ge₆ and TbFe₆Ge₆ (Left panel, straight line), and temperature dependence of the 4f contribution to the entropy $S_{4f}(T)$ (right axis, dashed lines). Dotted lines represent extrapolation to temperature T=0.

this material even more firmly in the "'d-electron heavy fermion" category [43–46]. The Debye temperature, estimated from β using the relation $\Theta_D = \left(\frac{12\pi^4 rR}{5\beta}\right)^{1/3}$, where r is the number of atoms per formula unit and R is the gas constant, is 486 K.

The C/T data for TbFe₆Ge₆, shown in Fig. 7(b), exhibits a broad lambda-like anomaly centered at 9 K, consistent with the reported magnetic ordering temperature of this compound and our susceptibility and resistivity measurements. In contrast, DyFe₆Ge₆ shows two distinct peaks in C/T, corresponding to the two magnetic transitions observed in susceptibility and resistivity measurements. The first peak at 8.6 K is broad and small, while the second one, at 5.8 K, is sharp and prominent. This difference in the magnetic ordering between the Tb and Dy compounds can be understood by analyzing the entropy released at the respective magnetic transition temperatures.

To isolate the magnetic contribution from the 4f

electrons, the 4f component of the heat capacity, C_{4f}/T , was extracted by subtracting the corresponding C/T data of the reference compound YFe₆Ge₆ with nonmagnetic R atom from those of TbFe₆Ge₆ and DyFe₆Ge₆ [54], as shown in Fig. 7(d), and the 4f-electron magnetic entropy, S_{4f} , was calculated by using $S_{4f} = \int_0^T (C_{4f}/T')dT'$. In DyFe₆Ge₆, an entropy of $R \ln 2$, corresponding to the first crystal field doublet among its eight Kramers doublets, is released just above the lower-temperature transition at 5.8 K. Only a part of the additional $R \ln 2$ is released just above the 8.6 K transition. This indicates that one low-lying doublet is involved in the magnetic ordering below 5.5 K while the other double is partially involved in the transitions at 8.6 K.

While Dy^{3+} is a Kramers ion and thus always has doublet states, Tb^{3+} is a non-Kramers ion and does not possess symmetry-protected doublets. However, the observation that $R \ln 2$ entropy is released just above the Tb magnetic ordering temperature suggests the presence of a quasi-doublet. This quasi-doublet likely leads to the

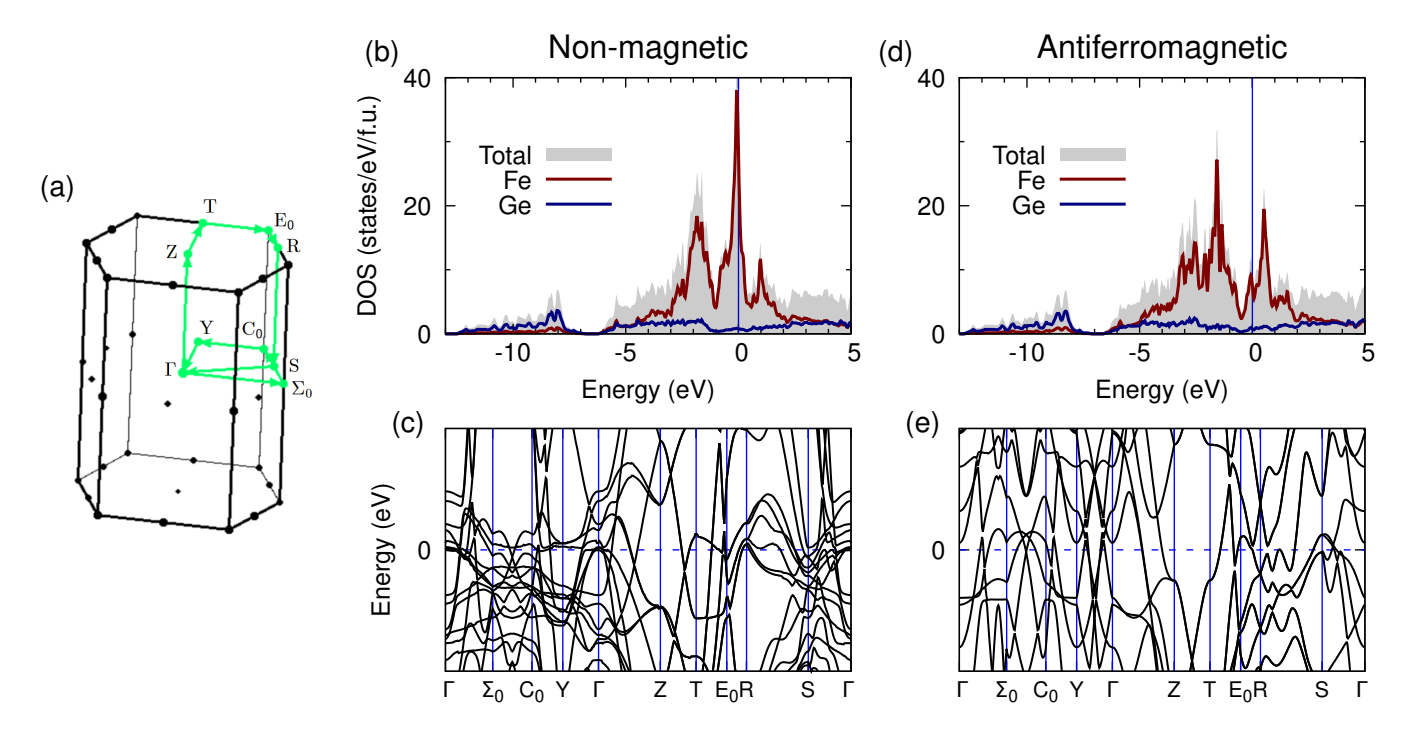


FIG. 8: First-principles electronic structure of YFe₆Ge₆. (a) The first Brillouin zone with highlighted high-symmetry points. (b, c) The density of states (DOS) and the band structure of YFe₆Ge₆ from a non-magnetic DFT calculation. (d,c) The DOS and the band structure of YFe₆Ge₆ from an antiferromagnetic DFT calculation. This antiferromagnetic phase corresponds to ferromagnetic kagome Fe planes that are coupled antiferromagnetically.

reduced and broadened heat capacity anomaly observed in ${\rm TbFe_6Ge_6}$, similar to the partially filled second double in ${\rm DyFe_6Ge_6}$.

E. First-principles calculations

Now, let us focus on the properties of the Fe magnetic sublattice of RFe₆Ge₆. Therefore, we will use the results obtained for YFe₆Ge₆, where Y is nonmagnetic, to present and discuss our findings. We found that the non-magnetic (NM) DFT state of YFe₆Ge₆ is higher in energy by about 250 meV per Fe compared to a magnetically-polarized state with ferromagnetically (FM) ordered Fe moments. Between the two considered magnetically-polarized states, the FM one and an antiferromagnetic (AFM) one with ferromagnetic kagome Fe planes coupled antiferromagnetically, the latter has a lower energy by 20 meV per Fe. This is in agreement with the experimentally determined magnetic ground state of the Fe sublattice in RFe₆Ge₆. We find the Fe magnetic moment to be very close to 2 $\mu_{\rm B}$. The considerable energy lowering upon spin polarization can be related to the sharp peak in the NM density of states (DOS) [Fig. 8(b)] at the Fermi level, $E_{\rm F}$, which is substantially reduced in the spin-polarized phases [Fig. 8(d)]. It is important to note that, as one can see in Figs. 8(b,d), the states near the Fermi level are predominantly of Fe character. Near the Fermi-energy $E_{\rm F}$ the band structure of $R{\rm Fe}_6{\rm Ge}_6$

as well as their Fermi surface remain complicated and certainly three-dimensional even in the magnetic ground state, as suggested by comparing the NM and AFM band structures in Figs. 8(c,e).

Total energy calculations elucidate the origin of the intriguing orthorhombic distortion described above. DFT calculations find several different energy scales. First, introducing disorder along a one-dimensional (1D) a-axis chain (...Y-Ge₂-Y-Ge₂...) incurs a very large energy cost of the order of 1 eV, indicating that each individual chain can be assumed to be perfectly ordered. Second, the relative ordering of these chains within the bc plane is governed by a much smaller energy scale (of the order of 1 meV). Consequently, the problem can be effectively mapped onto a two-dimensional triangular Ising model (TIM), in which the spin states correspond to the presence of either Y or a Ge₂ dimer at a given site within a particular bc plane.

An antiferromagnetic interaction in this Ising system corresponds to an elastic energy penalty reflecting the preference of Y atoms to neighbor Ge₂ dimers, whereas a ferromagnetic interaction corresponds to a preference of the like neighbors. The ground state of the nearestneighbor TIM (with the zero net magnetization) consists of one-dimensional ferromagnetic chains ordered along one of the three hexagonal directions, as illustrated in Fig. 9(a). However, the experimentally observed "double stripe" arrangement shown in Figs. 1(b), and 9(b), is not favored within this nearest-neighbor approxima-

tion. Given that elastic interactions are intrinsically long-ranged, it is not surprising that the double stripe configuration can emerge as the ground state (specifically, it is realized when the nearest neighbor interaction is "ferroelastic" and the second-neighbor interaction is "antiferroelastic", estimated from our calculations to be close to -1.8 meV and 8 meV, respectively). Thus, the DFT calculations suggest the possibility of a considerable intraplanar disorder coexisting with perfect ordering along the a-axis and a well defined orthorhombic alignment. Experimentally resolving such a state would require diffuse X-ray scattering measurements and can be part of future investigations.

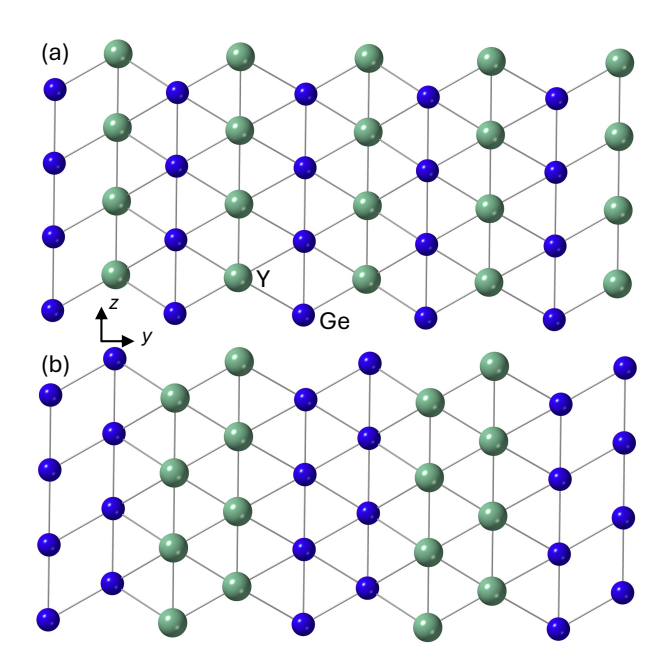


FIG. 9 : Triangular Ising Model. (a) 1D ferromagnetic chain structure of Y and Ge₂ dimers. (b) Double stripe structure of Y and Ge₂ dimers.

In future studies, it would be interesting to use first-principles calculations to explore in detail the rare-earth magnetism in $R\text{Fe}_6\text{Ge}_6$, taking advantage, for example, of the latest developments in DFT methodologies for treating strong correlation effects in f-electron ions[55]. Also, even though the experimentally determined crystal structures of $R\text{Fe}_6\text{Ge}_6$ are found to be stable and close to the theoretical equilibrium, positional disorder involving R atoms can potentially strongly affect magnetic properties at low temperatures and therefore deserves further

investigation.

V. CONCLUSION

In conclusion, single crystals of RFe₆Ge₆ (where R=Y, Dy, and Tb) are successfully synthesized, all crystallizing in an orthorhombic structure characterized by distorted kagome layers. The magnetic behavior of these compounds has been systematically investigated through magnetic susceptibility, isothermal magnetization, and magnetotransport measurements along different crystallographic directions. YFe₆Ge₆, which lacks of 4f electrons, exhibits a canted antiferromagnetic ordering. The magnetoresistance (MR) response in this compound reveals a negative MR both at low and high temperatures, indicating suppression of spin fluctuations in the system.

In contrast, TbFe₆Ge₆ demonstrates ferromagnetic behavior at low temperatures, as evidenced by both magnetic and transport measurements. DyFe₆Ge₆, on the other hand, displays a more complex magnetic behavior, likely due to the presence of partially filled 4f orbitals. The system exhibits two magnetic transitions at 5.8 K and 8.6 K, reflecting the coexistence of ferromagnetic and antiferromagnetic interactions. The MR behavior further corroborates this complexity, showing a positive MR below the Dy ordering temperature and a transition to negative MR above it, likely due to competing spin configurations. The progression from canted antiferromagnetism in YFe₆Ge₆ to ferromagnetism in TbFe₆Ge₆ and finally to a set of complex magnetic phases in DyFe₆Ge₆, highlights the critical role of the 4f electron configuration in tuning the magnetic ground state of the RFe₆Ge₆ family.

ACKNOWLEDGMENTS

N.J.G acknowledges the support from the NSF CA-REER award DMR-2343536. I. I. M. was supported by the National Science Foundation award No. DMR-2403804. M.P.G. acknowledges the University Grants Commission, Nepal for the financial support through Collaborative Research Grants (award no. CRG-78/79 S&T-03). M.P.G. thanks Ulrike Nitzsche for the technical assistance.

REFERENCES

^[1] R. Meduri, M. A. Plata, G. T. McCandless, B. C. Schundelmier, M. Ghafoor, K. Wei, and J. Y. Chan, Evolution of structural order and magnetic anisotropy in Yb_{0.5} (Co_{1-x}Fe_x)₃Ge₃ through doping of a kagome lattice, Chemistry of Materials (2025).

^[2] N. J. Ghimire and I. I. Mazin, Topology and correlations on the kagome lattice, Nature Materials 19, 137 (2020).

^[3] A. Bolens and N. Nagaosa, Topological states on the breathing kagome lattice, Physical Review B 99, 165141 (2019).

- [4] M. Hirschberger, T. Nakajima, S. Gao, L. Peng, A. Kikkawa, T. Kurumaji, M. Kriener, Y. Yamasaki, H. Sagayama, H. Nakao, et al., Skyrmion phase and competing magnetic orders on a breathing kagome lattice, Nature communications 10, 5831 (2019).
- [5] Y. Xie, K. Ji, J. He, X. Shen, D. Wang, and J. Zhang, Manipulation of topology by electric field in breathing kagome lattice, Physical Review Letters 135, 056701 (2025).
- [6] H. Bhandari, P.-H. Chang, R. B. Regmi, B. G. Markus, L. Forro, J. F. Mitchell, I. I. Mazin, and N. J. Ghimire, Tunable topological transitions in the frustrated magnet HoAgGe, Communications Materials 6, 52 (2025).
- [7] K. Zhao, Y. Tokiwa, H. Chen, and P. Gegenwart, Discrete degeneracies distinguished by the anomalous hall effect in a metallic kagome ice compound, Nature Physics 20, 442 (2024).
- [8] K. Zhao, H. Deng, H. Chen, K. A. Ross, V. Petricek, G. Gunther, M. Russina, V. Hutanu, and P. Gegenwart, Realization of the kagome spin ice state in a frustrated intermetallic compound, Science 367, 1218 (2020).
- [9] B. R. Ortiz, H. Miao, D. S. Parker, F. Yang, G. D. Samolyuk, E. M. Clements, A. Rajapitamahuni, T. Yilmaz, E. Vescovo, J. Yan, et al., Evolution of highly anisotropic magnetism in the titanium-based kagome metals LnTi₃Bi₄ (ln: La··· Gd³⁺, Eu²⁺, Yb²⁺), Chemistry of Materials 35, 9756 (2023).
- [10] A. P. Sakhya, B. R. Ortiz, B. Ghosh, M. Sprague, M. I. Mondal, M. Matzelle, I. Bin Elius, N. Valadez, D. G. Mandrus, A. Bansil, et al., Diverse electronic landscape of the kagome metal YbTi₃Bi₄, Communications Materials 5, 241 (2024).
- [11] P. Park, B. R. Ortiz, M. Sprague, A. P. Sakhya, S. A. Chen, M. D. Frontzek, W. Tian, R. Sibille, D. G. Mazzone, C. Tabata, et al., Spin density wave and van hove singularity in the kagome metal CeTi₃Bi₄, Nature Communications 16, 4384 (2025).
- [12] E. Cheng, K. Wang, Y. Hao, W. Chen, H. Tan, Z. Li, M. Wang, W. Gao, D. Wu, S. Sun, et al., Spectroscopic origin of giant anomalous hall effect in an interwoven magnetic kagome metal, arXiv preprint arXiv:2405.16831 (2024).
- [13] X. Yang, J. Pan, M. Yang, D. Chu, and S. Liu, Two-dimensional critical behavior, complex magnetic phase diagram, and anisotropic magnetic entropy change of a two-dimensional kagome magnet GdTi₃Bi₄, Journal of Magnetism and Magnetic Materials 621, 172916 (2025).
- [14] X. Han, H. Chen, Z. Cao, J. Guo, F. Fei, H. Tan, J. Guo, Y. Shi, R. Zhou, R. Wang, et al., Discovery of unconventional charge-spin-intertwined density wave in magnetic kagome metal GdTi₃Bi₄, arXiv preprint arXiv:2503.05545 (2025).
- [15] N. J. Ghimire, R. L. Dally, L. Poudel, D. Jones, D. Michel, N. T. Magar, M. Bleuel, M. A. McGuire, J. Jiang, J. Mitchell, et al., Competing magnetic phases and fluctuation-driven scalar spin chirality in the kagome metal YMn₆Sn₆, Science Advances 6, eabe2680 (2020).
- [16] Q. Wang, K. J. Neubauer, C. Duan, Q. Yin, S. Fujitsu, H. Hosono, F. Ye, R. Zhang, S. Chi, K. Krycka, et al., Field-induced topological hall effect and double-fan spin structure with ac-axis component in the metallic kagome antiferromagnetic compound YMn₆Sn₆, Physical Review B 103, 014416 (2021).

- [17] S. Roychowdhury, A. M. Ochs, S. N. Guin, K. Samanta, J. Noky, C. Shekhar, M. G. Vergniory, J. E. Goldberger, and C. Felser, Large room temperature anomalous transverse thermoelectric effect in kagome antiferromagnet YMn₆Sn₆, Advanced Materials 34, 2201350 (2022).
- [18] H. Li, H. Zhao, K. Jiang, Q. Wang, Q. Yin, N.-N. Zhao, K. Liu, Z. Wang, H. Lei, and I. Zeljkovic, Manipulation of dirac band curvature and momentum-dependent g factor in a kagome magnet, Nature Physics 18, 644 (2022).
- [19] A. Kitaori, N. Kanazawa, T. Yokouchi, F. Kagawa, N. Nagaosa, and Y. Tokura, Emergent electromagnetic induction beyond room temperature, Proceedings of the National Academy of Sciences 118, e2105422118 (2021).
- [20] H. Bhandari, R. L. Dally, P. E. Siegfried, R. B. Regmi, K. C. Rule, S. Chi, J. W. Lynn, I. Mazin, and N. J. Ghimire, Magnetism and fermiology of kagome magnet YMn₆Sn₄Ge₂, npj Quantum Materials 9, 6 (2024).
- [21] P. E. Siegfried, H. Bhandari, D. C. Jones, M. P. Ghimire, R. L. Dally, L. Poudel, M. Bleuel, J. W. Lynn, I. I. Mazin, and N. J. Ghimire, Magnetization-driven lifshitz transition and charge-spin coupling in the kagome metal YMn₆Sn₆, Communications Physics 5, 58 (2022).
- [22] Y. Zhu, D. Zhang, G. Zheng, K.-W. Chen, H. Bhandari, K. Jenkins, A. Chan, N. J. Ghimire, and L. Li, Geometrical nernst effect in the kagome magnet YMn₆ Sn₄Ge₂, Physical Review B 110, 195125 (2024).
- [23] H. Bhandari, Z. Ning, P.-H. Chang, P. E. Siegfried, R. B. Regmi, M. El. Gazzah, A. V. Davydov, A. G. Oliver, L. Ke, I. I. Mazin, et al., Three-dimensional nature of anomalous hall conductivity in YMn₆Sn_{6-x}Ga_x, x ≈ 0.55, npj Quantum Materials 10, 99 (2025).
- [24] D. C. Jones, S. Das, H. Bhandari, X. Liu, P. Siegfried, M. P. Ghimire, S. S. Tsirkin, I. Mazin, and N. J. Ghimire, Origin of spin reorientation and intrinsic anomalous hall effect in the kagome ferrimagnet TbMn₆Sn₆, Physical Review B 110, 115134 (2024).
- [25] S. Riberolles, T. J. Slade, R. Dally, P. Sarte, B. Li, T. Han, H. Lane, C. Stock, H. Bhandari, N. Ghimire, et al., Orbital character of the spin-reorientation transition in TbMn₆Sn₆, Nature Communications 14, 2658 (2023)
- [26] S. A. Ryan, A. Grafov, N. Li, H. T. Nembach, J. M. Shaw, H. Bhandari, T. Kafle, R. Sapkota, H. C. Kapteyn, N. J. Ghimire, et al., Uncovering the timescales of spin reorientation in TbMn₆Sn₆, arXiv preprint arXiv:2407.18894 (2024).
- [27] M. E. Gazzah, F. S. Yasin, S. Jamaluddin, H. Bhandari, R. B. Regmi, X. Yu, and N. J. Ghimire, Skyrmion bubbles by design in a centrosymmetric kagome magnet, arXiv preprint arXiv:2504.19045 (2025).
- [28] M. E. Gazzah, P.-H. Chang, Y. Lee, H. Bhandari, R. Regmi, X. Zhou, J. F. Mitchell, L. Ke, I. I. Mazin, and N. J. Ghimire, Doping-induced spin reorientation in kagome magnet TmMn₆Sn₆, arXiv preprint arXiv:2505.02936 (2025).
- [29] G. Dhakal, F. Cheenicode Kabeer, A. K. Pathak, F. Kabir, N. Poudel, R. Filippone, J. Casey, A. Pradhan Sakhya, S. Regmi, C. Sims, et al., Anisotropically large anomalous and topological hall effect in a kagome magnet, Physical Review B 104, L161115 (2021).
- [30] K. Fruhling, A. Streeter, S. Mardanya, X. Wang, P. Baral, O. Zaharko, I. I. Mazin, S. Chowdhury, W. D. Ratcliff, and F. Tafti, Topological hall effect induced by chiral fluctuations in ErMn₆Sn₆, Physical Review Mate-

- rials 8, 094411 (2024).
- [31] H. Zeng, G. Yu, X. Luo, C. Chen, C. Fang, S. Ma, Z. Mo, J. Shen, M. Yuan, and Z. Zhong, Large anomalous hall effect in kagome ferrimagnetic ErMn₆Sn₆ single crystal, Journal of Alloys and Compounds 899, 163356 (2022).
- [32] B. Wang, X.-F. Huang, D. Wu, H. Zuo, M. Wang, Y. Hou, and B. Shen, Unveiling the nontrivial electronic structures and fermi topology of high-temperature kagome ferrimagnet ErMn₆Sn₆, Nano Letters 24, 16031 (2024).
- [33] F. Kabir, R. Filippone, G. Dhakal, Y. Lee, N. Poudel, J. Casey, A. P. Sakhya, S. Regmi, R. Smith, P. Manfrinetti, et al., Unusual magnetic and transport properties in HoMn₆Sn₆ kagome magnet, Physical Review Materials 6, 064404 (2022).
- [34] H. W. S. Arachchige, W. R. Meier, M. Marshall, T. Matsuoka, R. Xue, M. A. McGuire, R. P. Hermann, H. Cao, and D. Mandrus, Charge density wave in kagome lattice intermetallic ScV₆Sn₆, Physical Review Letters 129, 216402 (2022).
- [35] G. Pokharel, B. Ortiz, J. Chamorro, P. Sarte, L. Kautzsch, G. Wu, J. Ruff, and S. D. Wilson, Highly anisotropic magnetism in the vanadium-based kagome metal TbV₆Sn₆, Physical Review Materials 6, 104202 (2022).
- [36] E. Rosenberg, J. M. DeStefano, Y. Guo, J. S. Oh, M. Hashimoto, D. Lu, R. J. Birgeneau, Y. Lee, L. Ke, M. Yi, et al., Uniaxial ferromagnetism in the kagome metal TbV₆Sn₆, Physical Review B 106, 115139 (2022).
- [37] S. Thomas, C. Kengle, W. Simeth, C.-y. Lim, Z. Riedel, K. Allen, A. Schmidt, M. Ruf, S. Gim, J. Thompson, et al., Unusual 5f magnetism in new kagome material UV₆Sn₆, npj Quantum Materials 10, 66 (2025).
- [38] O. Oleksyn, P. Schobinger-Papamantellos, J. Rodriguez-Carvajal, E. Bruck, and K. Buschow, Crystal structure and magnetic ordering in ErFe₆Ge₆ studied by x-ray, neutron diffraction and magnetic measurements, Journal of alloys and compounds 257, 36 (1997).
- [39] P. Schobinger-Papamantellos, O. Oleksyn, J. Rodriguez-Carvajal, G. Andre, E. Bruck, and K. Buschow, Atomic disorder, magnetic order and phase transitions of TbFe₆Ge₆ studied by x-ray, neutron diffraction and magnetic measurements (i), Journal of magnetism and magnetic materials 182, 96 (1998).
- [40] P. Schobinger-Papamantellos, K. Buschow, F. De Boer, C. Ritter, O. Isnard, and F. Fauth, The fe ordering in RFe₆Ge₆ compounds with non-magnetic R (R= Y, Lu, Hf) studied by neutron diffraction and magnetic measurements, Journal of alloys and compounds 267, 59 (1998).
- [41] O. Zaharko, P. Schobinger-Papamantellos, J. Rodriuez-Carvajal, and K. Buschow, Magnetic ordering in HoFe₆Ge₆ studied by neutron diffraction, Journal of alloys and compounds 288, 50 (1999).

- [42] P. Larson and I. Mazin, Effect of lattice relaxation on magnetic anisotropy: Zr-doped Sm₂Co₁₇, Physical Review B 69, 012404 (2004).
- [43] R. Fisher, R. Ballou, J. Emerson, E. Lelievre-Berna, and N. Phillips, Low-temperature specific heat of YMn₂ in the paramagnetic and antiferromagnetic phases, International Journal of Modern Physics B 07, 830 (1993).
- [44] M. Shiga, H. Wada, Y. Nakamura, J. Deportes, B. Ouladdiaf, and K. R. A. Ziebeck, Giant spin fluctuations in Y_{0.97}Sc_{0.03}Mn₂, Journal of the Physical Society of Japan 57, 3141 (1988).
- [45] H. Kotegawa, M. Matsuda, F. Ye, Y. Tani, K. Uda, Y. Kuwata, H. Tou, E. Matsuoka, H. Sugawara, T. Sakurai, H. Ohta, H. Harima, K. Takeda, J. Hayashi, S. Araki, and T. C. Kobayashi, Helimagnetic structure and heavyfermion-like behavior in the vicinity of the quantum critical point in mn₃P, Phys. Rev. Lett. 124, 087202 (2020).
- [46] Z. T. Messegee, V. O. Garlea, I. I. Mazin, S. H. Shin, Y. Xin, H. Bhandari, S. Calder, R. B. Regmi, N. J. Ghimire, J. I. Jang, and X. Tan, d-electron heavy fermion behavior in a near-room-temperature polar metallic ferrimagnet: A case of Mn₅SiC, Chemistry of Materials 37, 4832 (2025).
- [47] Bruker AXS, APEX-4, Bruker AXS, Madison, Wisconsin, USA (2021).
- [48] L. Krause, R. Herbst-Irmer, G. M. Sheldrick, and D. Stalke, Journal of applied crystallography, Journal of Applied Crystallography 48, 3 (2015).
- [49] G. M. Sheldrick, Shelxt-integrated space-group and crystal-structure determination, Foundations of Crystallography 71, 3 (2015).
- [50] P. Blaha, K. Schwarz, F. Tran, R. Laskowski, G. K. H. Madsen, and L. D. Marks, Wien2k: An APW+lo program for calculating the properties of solids, The Journal of Chemical Physics 152, 074101 (2020).
- [51] J. P. Perdew, K. Burke, and M. Ernzerhof, Generalized gradient approximation made simple, Phys. Rev. Lett. 77, 3865 (1996).
- [52] J. Cadogan, D. Ryan, I. Swainson, and O. Moze, The magnetic structure of YFe₆Ge₆, Journal of Physics: Condensed Matter 10, 5383 (1998).
- [53] J. Cadogan, D. Ryan, and I. Swainson, Neutron diffraction determination of the magnetic structure of DyFe₆Ge₆, Journal of Physics: Condensed Matter 12, 8963 (2000).
- [54] N. Ghimire, S. Cary, S. Eley, N. Wakeham, P. Rosa, T. Albrecht-Schmitt, Y. Lee, M. Janoschek, C. Brown, L. Civale, et al., Physical properties of the Ce₂MAl₇Ge₄ heavy-fermion compounds (M= Co, Ir, Ni, Pd), Physical Review B 93, 205141 (2016).
- [55] Y. Lee, Z. Ning, R. Flint, R. J. McQueeney, I. I. Mazin, and L. Ke, Importance of enforcing hund's rules in density functional theory calculations of rare earth magnetocrystalline anisotropy, npj Computational Materials 11 (2025).

APPENDIX: ADDITIONAL DATA

The reproduced datasets of magnetization, electrical resistivity, magnetoresistance, and heat capacity for the $R\text{Fe}_6\text{Ge}_6$ (R = Y, Tb, Dy) series, obtained from a newly synthesized batch of single crystals grown independently, exhibit excellent agreement with previously reported experimental results. This consistency confirms the high reproducibility and reliability of the growth process as well as the stability of the intrinsic magnetic and electronic properties

across different sample batches. To reproduce and reverify the unusual behavior of specific heat of YFe₆Ge₆ in C/T vs. T^2 , multiple batch of sample has been grown and in Fig. 15(a,b) confirms its reproducibility in different batch of samples and from batch 2 sample 2 γ value was found to be 94 mJ·mol-F.U.⁻¹·K⁻² and from batch 3 sample 3 it was found to be 99 mJ·mol-F.U.⁻¹·K⁻². Similarly β was calculated as 0.27 mJ·mol-F.U.⁻¹·K⁻⁴ and 0.25 mJ·mol-F.U.⁻¹·K⁻⁴ respectively which matches well with the previously calculated values.

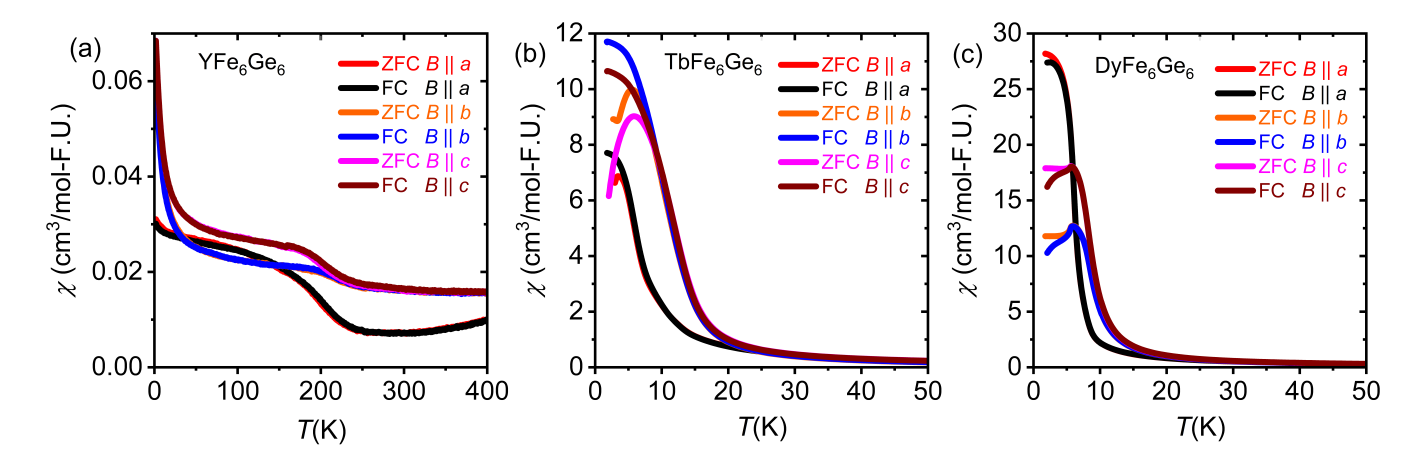


FIG. 10: Temperature dependence magnetic susceptibility (FC, ZFC) measured at 0.1 T magnetic field in all three crystallographic directions for a) YFe₆Ge₆, b) TbFe₆Ge₆ and c) DyFe₆Ge₆.

TABLE III: Atomic coordinates, occupancy, isotropic displacement parameters, and Wyckoff sites for TbFe₆Ge₆ compounds.

Atom	Site	Occ.	x	y	z	$\mathrm{U}(_{eq})$
Tb(1)	4c	1.000	1.00000	0.37278	0.25000	0.006
Ge(1)	8g	1.000	0.65304	0.37538	0.25000	0.005
Ge(2)	4c	1.000	1.00000	0.45803	0.75000	0.006
Ge(3)	4c	1.000	0.50000	0.54045	0.25000	0.005
Ge(4)	4c	1.000	0.50000	0.29510	0.75000	0.006
Ge(5)	4c	1.000	0.50000	0.21054	0.25000	0.006
Fe(1)	8d	1.000	0.25000	0.25000	0.50000	0.005
Fe(2)	8g	1.000	0.74975	0.37500	0.75000	0.005
Fe(3)	8e	1.000	0.75065	0.50000	0.50000	0.005

TABLE IV: Atomic coordinates, occupancy, isotropic displacement parameters, and Wyckoff sites for DyFe₆Ge₆ compounds.

Atom	Site	Occ.	x	y	z	U(eq)
Dy(1)	4c	1.000	0.00000	0.62729	0.75000	0.006
Ge(1)	8g	1.000	0.34713	0.62468	0.75000	0.007
Ge(2)	4c	1.000	0.00000	0.54201	0.25000	0.006
Ge(3)	4c	1.000	0.50000	0.70488	0.25000	0.007
Ge(4)	4c	1.000	0.50000	0.78947	0.75000	0.007
Ge(5)	4c	1.000	0.50000	0.45961	0.75000	0.007
Fe(1)	8e	1.000	0.24961	0.50000	0.50000	0.007
Fe(2)	8g	1.000	0.25046	0.62494	0.25000	0.007
Fe(3)	8d	1.000	0.75000	0.75000	0.50000	0.007

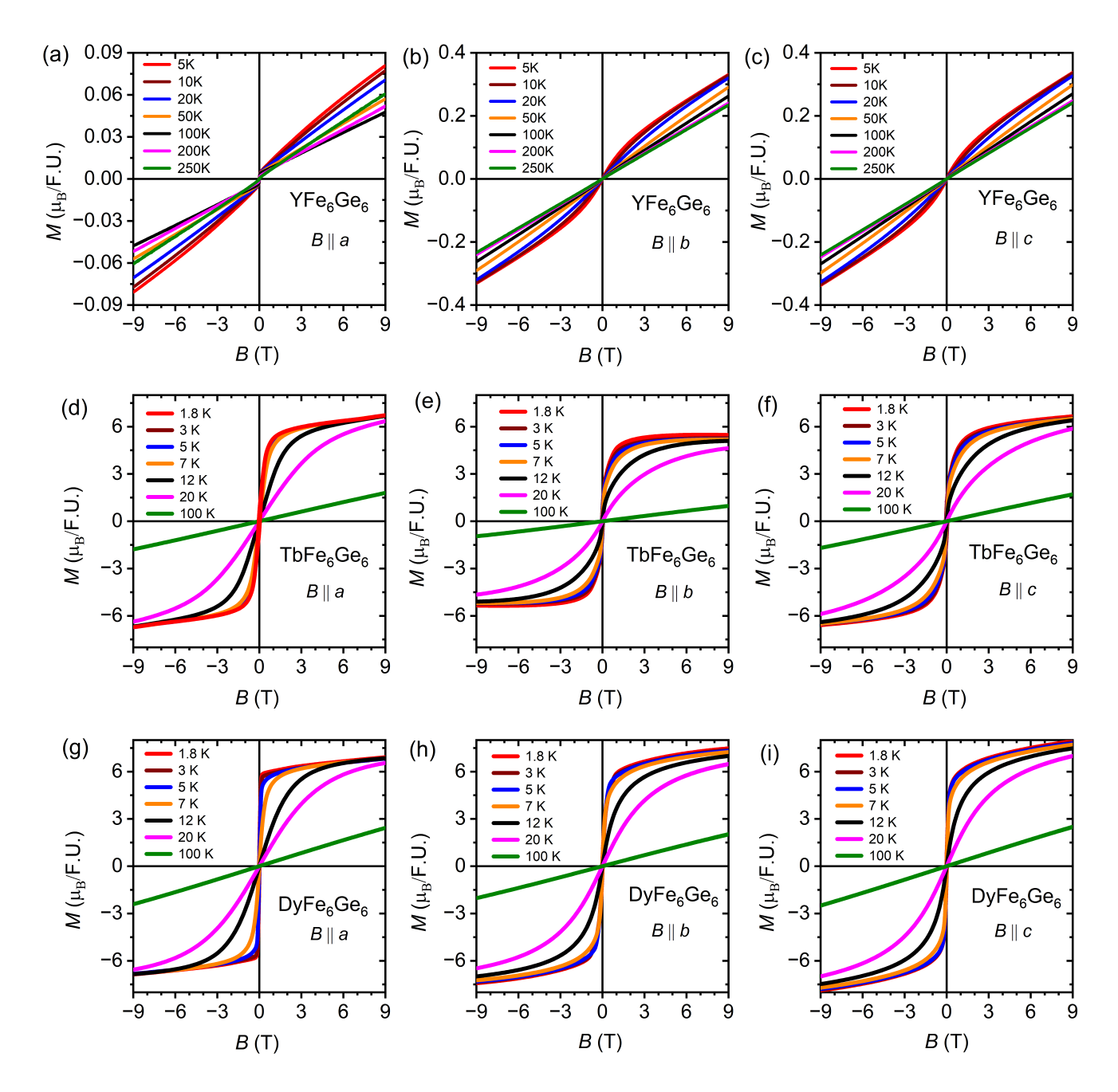


FIG. 11 : Field-dependent isothermal magnetization (M vs. B) measurements were carried out along the crystallographic a, b, and c axes for three compounds: (a–c) YFe₆Ge₆, (d–f) TbFe₆Ge₆, and (g–i) DyFe₆Ge₆. Data were reproduced using a different batch of single-crystalline samples to ensure consistency and reproducibility. The measurements were performed at selected temperatures under an external magnetic field varying from 9 T to –9 T and –9 T to 9 T.

TABLE V : Crystallographic parameters for $R\text{Fe}_6\text{Ge}_6$ compounds ($R=\text{Tb},\,\text{Dy},\,\text{Y}$) at 250(2) K using Mo K α radiation.

Crystal system			Ortho	rhombic						
Space group	Cmcm									
Temperature (K)	250(2)									
Wavelength (Å)				1073						
Z (formula units)			0.,	2						
$2\theta_{\min}$ (°)			4	.61						
$2\theta_{\rm max}$ (°)				5.59						
Index ranges	-10 < h < 10, -23 < k < 23, -6 < l < 6									
Compounds	YFe_6Ge_6 10%	$YFe_{6}Ge_{6}20\%$	$\mathrm{TbFe_{6}Ge_{6}10\%}$	$\mathrm{TbFe_{6}Ge_{6}20\%}$	$\overline{\text{DyFe}_6\text{Ge}_610\%}$	$\mathrm{DyFe_{6}Ge_{6}20\%}$				
Formula weight	1719.10	1719.10	1859.12	1859.12	1866.28	1866.28				
a (Å)	8.1134(3)	8.1134(3)	8.1379(3)	8.1379(3)	8.1193(2)	8.1193(2)				
b (Å)	17.6662(7)	17.6662(7)	17.6975(6)	17.6975(6)	17.6699(6)	17.6699(6)				
c (Å)	5.11650(10)	5.11650(10)	5.1257(2)	5.1257(2)	5.11910(10)	5.11910(10)				
Volume (Å ³)	733.36(4)	733.36(4)	738.21(5)	738.21(5)	734.42(3)	734.42(3)				
Density (calc., g/cm ³)	$7.78\hat{5}$	$7.78\overline{5}$	8.364	8.365	8.439	8.439				
$\mu \text{ (Mo K}\alpha) \text{ (cm}^{-1})$	433.73	433.73	447.68	447.68	455.43	455.43				
Goodness of fit on F^2	2.406	2.393	1.206	1.138	5.081	4.627				
$R(F)$ for $F^2 > 2\sigma(F^2)^a$	0.1418	0.1659	0.0378	0.0741	0.2904	0.3162				
$R_w(F^2)^{\mathrm{b}}$	0.4751	0.4737	0.1132	0.2185	0.7058	0.6835				

TABLE VI : Atomic coordinates, occupancy, isotropic displacement parameters, and Wyckoff sites for YFe $_6$ Ge $_6$ compounds with 10% and 20% disorder.

Atom	Site	Occ.10%	Occ.20%	x	y	z	U(eq) 10%	U(eq) 20%
Y(1)	4c	0.890	0.800	0.00000	0.62710	0.75000	0.030	0.037
Y(1)	4c	0.110	0.200	0.50000	0.62710	0.75000	-0.001	0.016
Ge(1)	8g	0.890	0.800	0.34708	0.62470	0.75000	0.021	0.024
Ge(1)	8g	0.110	0.200	0.84708	0.62470	0.75000	-0.037	-0.001
Ge(2)	4c	1.000	1.000	0.00000	0.54202	0.25000	0.024	0.027
Ge(3)	4c	1.000	1.000	0.50000	0.70505	0.25000	0.018	0.022
Ge(4)	4c	1.000	1.000	0.50000	0.78957	0.75000	0.021	0.025
Ge(5)	4c	1.000	1.000	0.50000	0.45955	0.75000	0.015	0.019
Fe(1)	8e	1.000	1.000	0.24959	0.50000	0.50000	0.021	0.024
Fe(2)	8g	1.000	1.000	0.25036	0.62496	0.25000	0.021	0.025
Fe(3)	8d	1.000	1.000	0.75000	0.75000	0.50000	0.021	0.024

TABLE VII : Atomic coordinates, occupancy, isotropic displacement parameters, and Wyckoff sites for TbFe $_6$ Ge $_6$ compounds with 10% and 20% disorder.

Atom	Site	Occ.10%	Occ.20%	x	y	z	$U(_{eq})$ 10%	U(eq) 20%
Tb(1)	4c	0.890	0.800	1.00000	0.37278	0.25000	0.007	0.007
Tb(1)	4c	0.110	0.200	0.50000	0.37278	0.25000	0.044	0.055
Ge(1)	8g	0.890	0.800	0.65304	0.37538	0.25000	0.006	0.006
Ge(1)	8g	0.110	0.200	0.15304	0.37538	0.25000	0.047	0.046
Ge(2)	4c	1.000	1.000	1.00000	0.45803	0.75000	0.009	0.016
Ge(3)	4c	1.000	1.000	0.50000	0.54045	0.25000	0.009	0.016
Ge(4)	4c	1.000	1.000	0.50000	0.29510	0.75000	0.014	0.014
Ge(5)	4c	1.000	1.000	0.50000	0.21054	0.25000	0.014	0.015
Fe(1)	8d	1.000	1.000	0.25000	0.25000	0.50000	0.011	0.015
Fe(2)	8g	1.000	1.000	0.74975	0.37500	0.75000	0.010	0.015
Fe(3)	8e	1.000	1.000	0.75065	0.50000	0.50000	0.010	0.015

TABLE VIII : Atomic coordinates, occupancy, isotropic displacement parameters, and Wyckoff sites for DyFe $_6$ Ge $_6$ compounds with 10% and 20% disorder.

Atom	Site	Occ.10%	Occ.20%	x	y	z	$U(_{eq})$ 10%	$U(_{eq}) 20\%$
Dy(1)	4c	0.890	0.800	0.00000	0.62729	0.75000	0.303	0.076
Dy(1)	4c	0.110	0.200	0.50000	0.62729	0.75000	-0.304	0.066
Ge(1)	8g	0.890	0.800	0.34708	0.62468	0.75000	-0.291	-0.012
Ge(1)	8g	0.110	0.200	0.84708	0.62468	0.75000	0.347	-0.010
Ge(2)	4c	1.000	1.000	0.00000	0.54201	0.25000	-0.007	0.023
Ge(3)	4c	1.000	1.000	0.50000	0.70488	0.25000	-0.005	0.027
Ge(4)	4c	1.000	1.000	0.50000	0.78947	0.75000	-0.007	0.025
Ge(5)	4c	1.000	1.000	0.50000	0.45961	0.75000	-0.006	0.031
Fe(1)	8e	1.000	1.000	0.24961	0.50000	0.50000	-0.010	0.020
Fe(2)	8g	1.000	1.000	0.25046	0.62494	0.25000	-0.011	0.013
Fe(3)	8d	1.000	1.000	0.75000	0.75000	0.50000	0.000	0.020

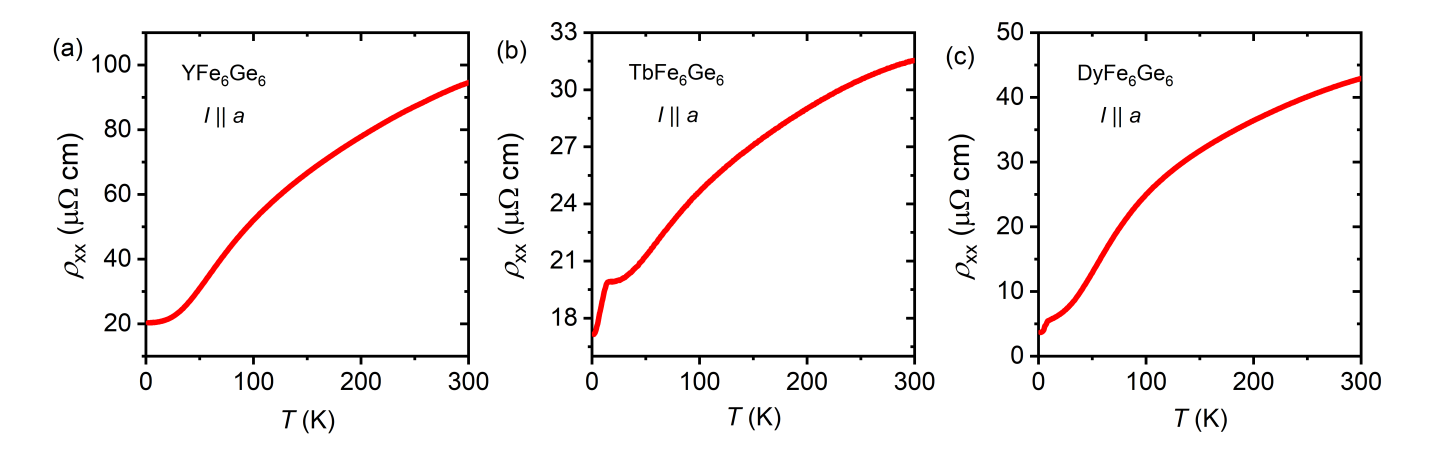


FIG. 12: Temperature-dependent longitudinal resistivity measurements were reproduced using a separate batch of single-crystalline samples for (a) YFe_6Ge_6 , (b) $TbFe_6Ge_6$, and (c) $DyFe_6Ge_6$. The measurements were performed following identical experimental protocols to ensure consistency and to validate the reproducibility of the transport behavior.

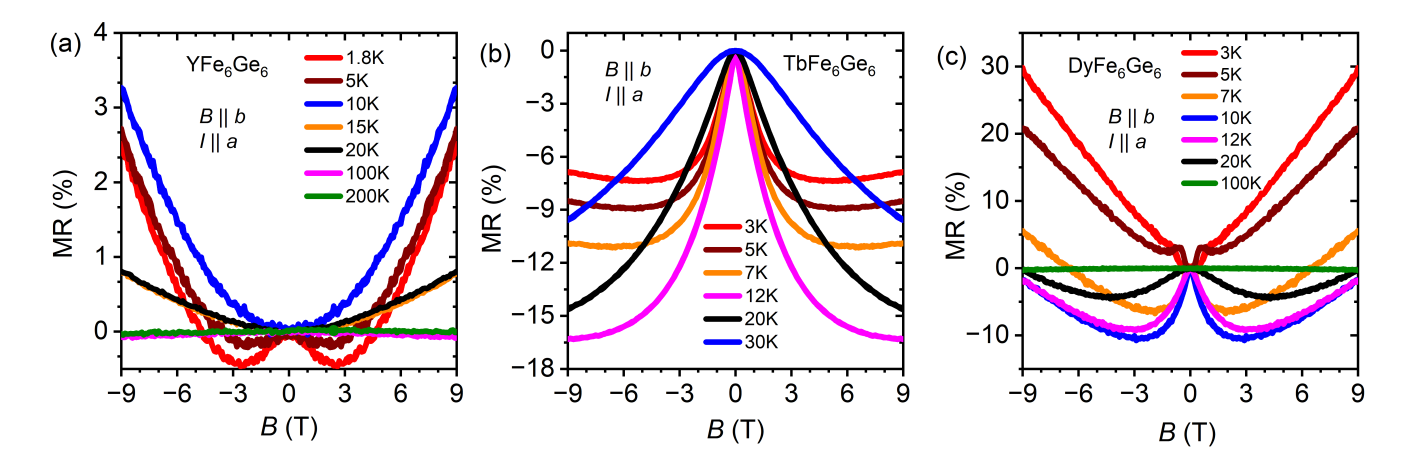


FIG. 13: Reproducibility of transverse magnetoresistance (MR) measurements was verified using a separate batch of samples for (a) YFe₆Ge₆, (b) DyFe₆Ge₆, and (c) TbFe₆Ge₆. The measurements were conducted following the same experimental configuration and protocols to ensure consistency across different sample batches.

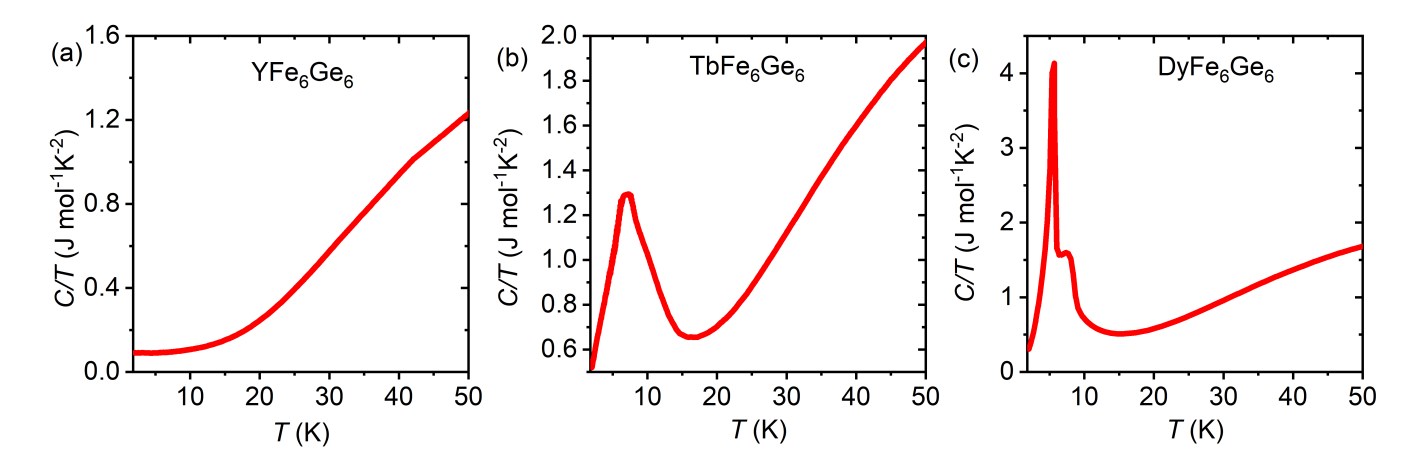


FIG. 14: Reproducibility of specific heat measurements, plotted as C/T versus temperature, was confirmed using a separate batch of samples for (a) YFe₆Ge₆, (b) TbFe₆Ge₆, and (c) DyFe₆Ge₆. All measurements were performed under identical conditions to ensure consistency and to validate the intrinsic thermodynamic behavior of each compound.

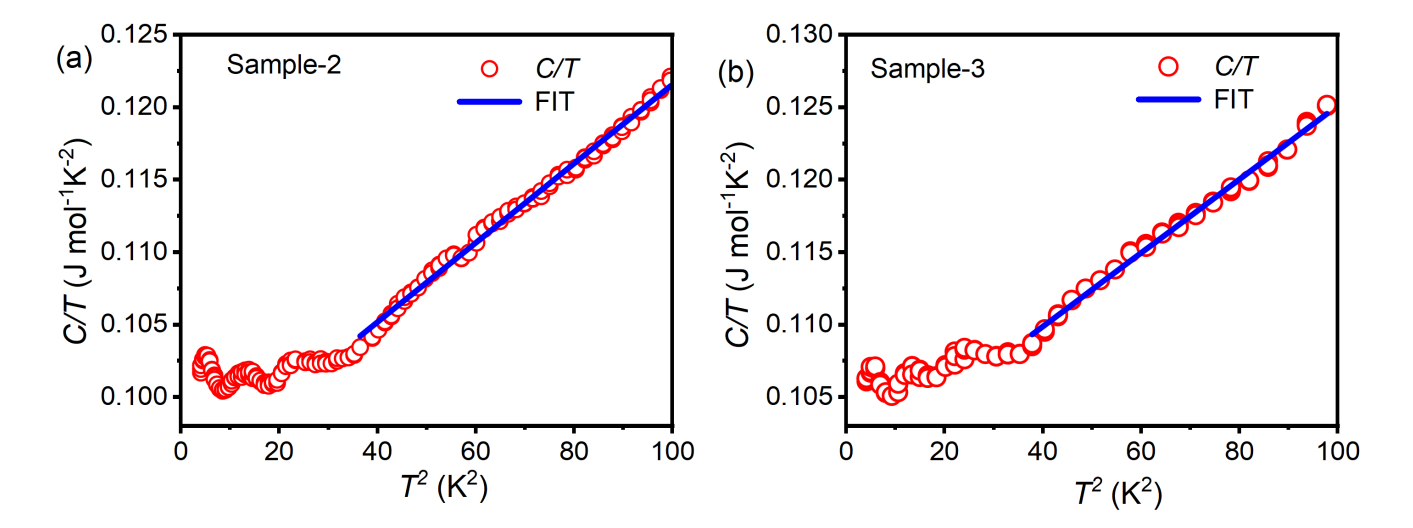


FIG. 15: Reverification of specific heat measurements from different batch of YFe₆Ge₆ from 1.8K to 10K and plotted as C/T versus $T^2(\mathbf{a})$ sample 2 from batch 2, (b) sample 3 from batch 3.